Supporting Information for

Tailoring Lewis Acid Sites in Lanthanum-Doped Carbon Nitride for H_2O_2 Synthesis and Efficient Photocatalytic Degradation of Antibiotics

Xiaojuan Bai[*a,b], Wenzhi Zhang[b], Jiaqian Dong[b], Chi Zhang[b]

[a] Key Laboratory of Urban Stormwater System and Water Environment, Ministry of Education, Beijing University of Civil Engineering and Architecture, Beijing 100044, China.

[b] Beijing Energy Conservation&Sustainable Urban and Rural Development Provincial and Ministry Co-construction Collaboration Innovation Center,Beijing University of Civil Engineering and Architecture,Beijing, China.

E-mail: baixiaojuan@bucea.edu.cn, heixia.1986@163.com (Xiaojuan Bai)

Experimental procedures

Supplementary Text 1. Materials

Thiourea (CH_4N_2S), lanthanum oxide (La_2O_3), methanol, and formic acid were purchased from Beijing Macklin Biochemical Co, Ltd; tetracycline, ciprofloxacin, chloramphenicol, sulfamethoxazole, sodium sulfate (Na_2SO_4), ammonium chloride (NH_4Cl), monopotassium phosphate (KH_2PO_4), and potassium nitrate (KNO_3) were purchased from Sinopharm Chemical Reagent Co, Ltd. All purchased reagents were of analytical grade or above and could be used directly without further purification. All reagents were used without further purification.

Supplementary Text 2

2.1 Preparation of g-C_3N_4

The synthesis followed previously reported methods[1].Typically,20 g of thiourea was ground in a mortar and then placed in a covered crucible. The crucible was heated in a muffle furnace under air at 5°C·min^{-1} to 550°C and held for 4 h. After cooling to room temperature, the product was ground in an agate mortar to obtain a light-yellow carbon nitride powder, referred to as g-C_3N_4.

2.2 Preparation of ORCN

ORCN was synthesized using a procedure analogous to g-C_3N_4, with La_2O_3 added at thiourea to La_2O_3 mass ratios of 300:1, 200:1, 100:1, 80:1, and 40:1. Among these, the sample with a 200:1 mass ratio showed the best performance and was designated as ORCN for further experiments.

Supplementary Text 3.Characterization of Photocatalysts

X-ray diffraction (XRD) patterns of the powder were recorded using a Smart Lab SE X-ray diffractometer (Cu Kαradiation) from Rigaku, Japan, to determine the structure of carbon nitride. On a JNM-ECZ600R solid-state nuclear magnetic resonance spectrometer, 13C cross-polarization magic-angle spinning (CP-MAS) solid-state NMR spectra were recorded using a 3.2 mm magic-angle spinning probe.

Use the SU-8010 scanning electron microscope to observe the appearance of the sample, combining it with scanning electron microscopy (SEM) and energy dispersive spectroscopy (EDS) analysis. Capture transmission electron microscopy (TEM) images using the HT7700 transmission electron microscope. Measure the Brunauer-Emmett-Teller (BET) specific surface area of carbon nitride via nitrogen adsorption-desorption isotherms at 573K using the BSD-660MA6M instrument. Electrochemical tests were conducted on a CHI-660E electrochemical workstation. Analyze the zeta potential of carbon nitride using the Zeta sizer 26 Nano ZS90 (Malvern, UK). Steady-state/transient fluorescence spectra were obtained using an Edinburgh FLS1000 (UK). Perform X-ray photoelectron spectroscopy (XPS) analysis of carbon nitride using the ESCALAB Xi (Thermo Fisher Scientific, USA). Measure electron

paramagnetic resonance (EPR) spectra at room temperature using the ESR 300E spectrometer (Bruker, Germany).

Using the UV3600PLUS spectrophotometer (Shimadzu, Japan), with barium sulfate as the reference, the UV-visible diffuse reflectance spectra (UV-vis DRS) of the dry pressed samples were recorded. The optical band gap (Eg) was calculated using the following equation:

$(\alpha \cdot h\nu)^{1/n}=B\ (h\nu-Eg)$

Here,α is the absorption coefficient, h is Planck's constant, ν is the light frequency, B is a constant, and Eg is the corresponding band gap. In addition, the factor n is determined by the nature of the electronic transition. Specifically, n=1/2 indicates a direct band gap transition, while n=2 indicates an indirect band gap transition. In this study, since carbon nitride has direct transition characteristics, its n value is equal to 1/2.

The degradation efficiency of tetracycline, ciprofloxacin, and diclofenac sodium was measured using Acquity UPLC H-Class (Waters, USA). The mobile phase for SMX consisted of methanol and 0.1% formic acid solution (40:60, v/v) at a flow rate of 0.4 ml/min, and a UV detector was used.

Supplementary Text 4.Photocurrent Measurement

The transient photocurrent response experiment was conducted using the CHI660E electrochemical system in a three-electrode setup.10 mg of the catalyst were dispersed in 1 mL of a solvent mixture consisting of 0.5 mL ultrapure water and 0.5 mL ethanol, followed by ultrasonication for 30 min to form a homogeneous suspension.Subsequently,150μL of this suspension was drop-cast onto an ITO glass substrate and dried at ambient temperature prior to testing. The sample was coated on indium tin oxide (ITO) glass. A Pt wire electrode and a saturated calomel electrode were used as the working electrode, counter electrode, and reference electrode, respectively. A 0.1 M Na_2SO_4 solution was used as the electrolyte.

Supplementary Text 5. Photocatalytic Production

Disperse 5 mg of photocatalyst in 25 ml of aqueous solution. Then, sonicate the dispersion for 5 minutes and continuously stir for 30 minutes. All photocatalytic reactions are carried out in an air atmosphere under irradiation by a 300 W xenon lamp. Every 10 minutes, remove 1.5 mL of the solution and filter it through a 0.45μm filter into a centrifuge tube. Add 0.5 ml of 0.1 mol/L potassium hydrogen phthalate (CHKO) aqueous solution and 0.5 ml of 0.4 mol/L potassium iodide (KI) aqueous solution to the solution, and let it stand for 30 minutes.

Under acidic conditions ($H_2O_2+3I^-+2H^+\rightarrow I_3^-+2H_2O$), H_2O_2 molecules react with iodide ions (I^-) to produce trivalent iodine ions (I_3^-), which have strong absorption near 350 nm^2. The amount of I_3^- can be determined using UV-Visible spectroscopy, and the amount of H_2O_2

generated in each reaction can be estimated based on the absorbance at 350 nm. Known concentrations of H_2O_2 are added to KI and CHKO solutions, and measurements are taken using a UV-Visible spectrophotometer to obtain a calibration curve, as described below.

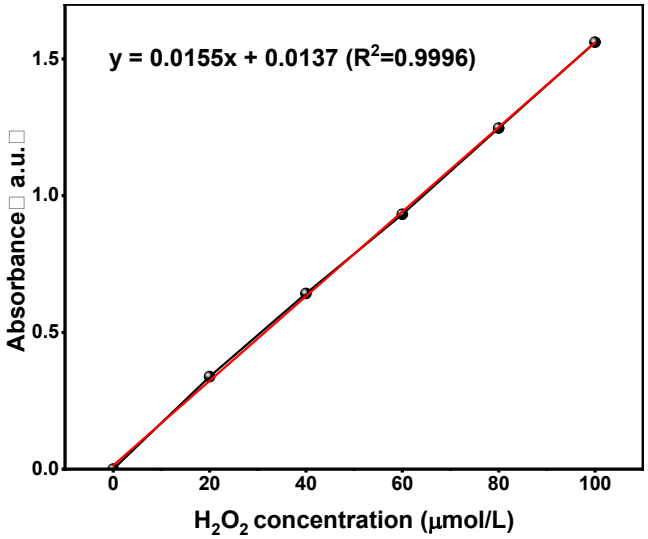

Supplementary Figure 1. Calibration curve of H_2O_2 concentration determined by UV spectrophotometry.

Amount of H_2O_2 accumulation: $[H_2O_2]=K_f \div K_d(1-e^{-kdt})$ (Eq. S1)

The hydrogen peroxide production capacity of the synthesized materials after screening is shown in the figure below, which will not be elaborated on in the main text and subsequent sections. The material with the best performance (200:1) is selected as ORCN.

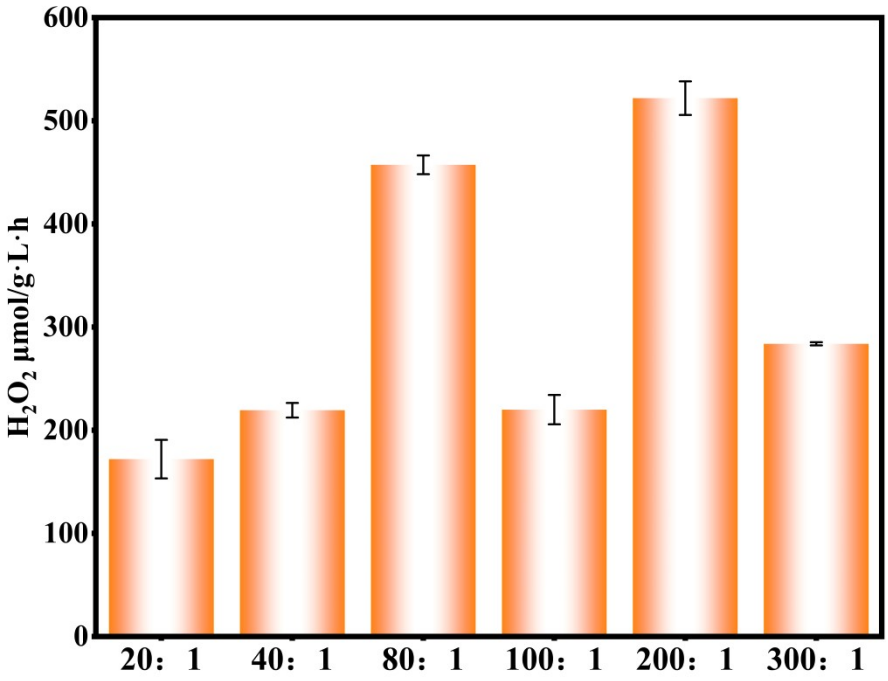

Supplementary Figure 2. H_2O_2 generation rates for materials with varying ratios

Supplementary Text 6. Quantitative Experiments of Free Radicals.

Determination of free $\bullet O_2^-$ concentration. Nitroblue tetrazolium (NBT) could be reduced by •O2- to blue formazan, and 1 mol NBT can react with 4 mol $\bullet O_2^-$. The concentration of generated •O2- is quantified by measuring the residual concentration of NBT on a UV-vis spectrophotometer (maximum absorbance at 259 nm).

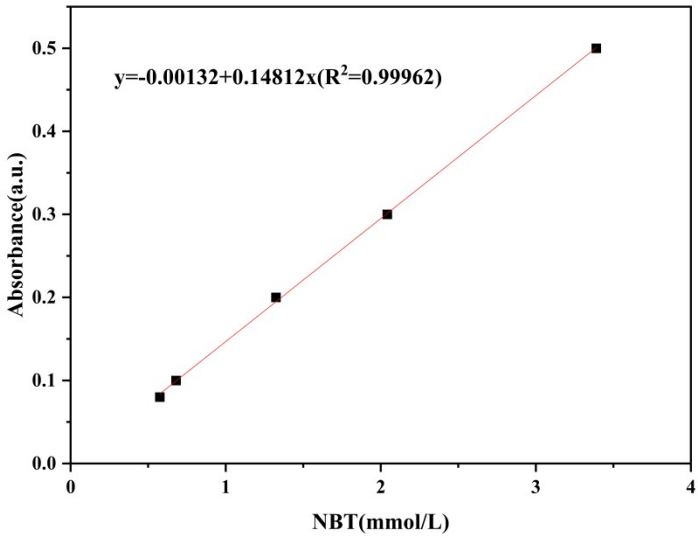

Supplementary Figure 3. Calibration curve of nitroblue tetrazolium (NBT) concentration

Relative quantification of •OH by benzoic acid (BA) method

BA could react with •OH to produce o-hydroxybenzoic acid (o-HBA), m-HBA, and p-HBA with a yield ratio of 1.7 : 2.3 : 1.2, the three products account for 90 ± 5% of the reaction (Eq. S1). Typically, 5.87 ± 0.18 moles •OH react with BA could produce one-mole p-HBA, and the concentration of p-HBA is easily determined by the high-performance liquid chromatography (HPLC), therefore, the generation of p-HBA could be used to quantify the concentration of cumulative •OH (Eq. S2)[3]. The initial BA concentration was employed as 10 mmol · L^{-1} except for a specific statement.

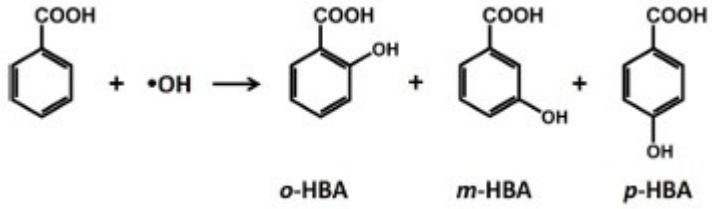

(Eq. S2)

Cumulative [•OH] = 5.87 × [p-HBA] (Eq. S3)

Supplementary Text 7. Experimental Water Sample

Collect water from the lake on the campus of Beijing University of Civil Engineering and Architecture (BUCEA). The simulated water is prepared based on the pollutant concentrations of the actual water samples and follows the "Groundwater Quality Standards" with reference to the pollutant limits specified in the "Groundwater Quality Standards" (GB/T 14848-2017) and the "Environmental Quality Standards for Surface Water "(GB 3838-2002). The concentrations of added inorganic anions are adjusted according to the limits specified in these standards.

Supplementary Text 8. **Apparent Quantum Yield (AQY) and Solar-to-Chemical Conversion (SCC)**

Under the xenon lamp light source(PL-SXE300D,Beijing Bofeilai Technology),using different bandpass filters (380nm, 420nm, 450nm, 500nm, and 550nm), the light power corresponding to monochromatic light was measured with a light power meter (PL-MW2000, Beijing Bofeilai Technology). The formula for calculating the apparent quantum yield (AQY) is as follows:

$$AQY(\%) = \frac{(number\ of\ produced\ H_2O_2\ molecules) \times 2}{number\ of\ incident\ photons} \times 100\%$$

number of produced H_2O_2 molecules = $C_{H_2O_2} \times N_A$

Incident photon number:

$$N_{incident} = \frac{t}{h\nu} = \frac{Pt\lambda}{hc} = \frac{ISt\lambda}{hc}$$

Where N_A=6.022×10^{23} units/mol; I is the optical power intensity(W·m^{-2}); S is the irradiated area (m^2); t is the reaction time(s); λ is the wavelength length of monochromatic light(m); h is Planck's constant(6.63×10^{-34} m^2 kg s^{-1}); and c is the speed of light in free space (3.0×10^8 m·s^{-1}). (Units: 1 W=1 J/s, 1 J=1 kg·m^2/s^2).

The solar-to-chemical energy conversion (SCC) efficiency measurement for H_2O_2 evolution was performed under an AM 1.5G solar simulator (100 mW·cm^{-2}) equipped with a λ>420 nm cutoff filter illumination. The concentration of the catalyst is 0.2 g·L^{-1}. Calculated the SCC efficiency(η)via the following equation:

$$\eta = \frac{\Delta G(H_2O_2 \times n(H_2O_2)}{t_{ir} \times S_{ir} \times I_{AM}} \times 100\%$$

In the equation, △G(H_2O_2)=117 kJ·mol^{-1}, is the free energy for H_2O_2 generation. n(H_2O_2) is the amount of H_2O_2 generated during the photocatalytic reaction. The irradiation time tir is 3600s, and the irradiated sample area (S_{ir}) is 2.12×10^{-3} m^2. I_{AM},the total irradiation intensity of the AM 1.5 global spectra (300nm-2500nm), is 100 mw·cm^{-2}.

Supplementary Text 9. Quantitative Experiments of Free Radicals.

Determination of free •O_2^- concentration. Nitroblue tetrazolium (NBT) could be reduced by •O_2^- to blue formazan, and 1 mol NBT can react with 4 mol •O_2^-. The concentration of generated •O_2^- is quantified by measuring the residual concentration of NBT on a UV-vis

spectrophotometer (maximum absorbance at 259 nm).

Determination of free •OH concentration. Benzoic acid (BA) can be oxidized by •OH to hydroxylated products (2-HBA, 3-HBA, 4-HBA, 2,5-DHBA). The concentration of generated •OH is quantified by measuring the formation concentration of hydroxylated products on high-performance liquid chromatography (Eq.1).

$$\text{RhB } [\bullet OH] = [\text{2-HBA}] + [\text{3-HBA}] + [\text{4-HBA}] + 2 \times [\text{2,5-DHBA}]$$

Supplementary Text 10.TG-DSC

TG-DSC was performed on a HITACHI STA200 instrument in Japan under a nitrogen gas atmosphere,with a heating range of 30–800°C and a heating rate of 10°C/min.

Supplementary Text 11.Pyridine FTIR

Py-IR spectra were recorded on a Bruker Tensor 27 FTIR spectrometer (Germany) to probe Brønsted and Lewis acid sites on C-N-La catalyst samples.Samples were prepared as KBr pellets (~1–2 wt%loading, ~13 mm diameter, ~1 mm thickness) and pretreated in situ under vacuum ($<10^{-3}$ mbar) at 150°C for 1 h to remove physisorbed water. Pyridine vapor was adsorbed at room temperature (25°C, 0.1–1 mbar partial pressure) until saturation (30min), followed by evacuation of excess physisorbate.

Desorption spectra were collected at 100°C, 150°C, and 200°C (ramp rate: 5°C/min, equilibration: 10 min each), with 64 scans averaged at 4 cm^{-1} resolution over 400–4000 cm^{-1}. Background subtracted at 150°C.

Acid site quantities (μmol/g) were calculated using integrated peak areas (A,cm^{-1}) at 1450 $cm^{-1}$and 1611 cm^{-1},normalized for sample mass (m, mg):

$$\text{Lewis acid amount} = 1.42 \times A_L \times 1.3 \times 1.3/m/4 \times 1000$$

$$\text{Brønsted acid amount} = 1.88 \times A_B \times 1.3 \times 1.3/m/4 \times 1000$$

$$\text{Total acid amount} = \text{Lewis} + \text{Brønsted}$$

A_L:Lewis acid area

A_B;Brønsted acid area

Supplementary text 12. Photocatalytic activity evaluation in continuous flow system

The continuous flow photodegradation testing was conducted within a straightforward dynamic reactor system, as illustrated in Figure S10. The procedure encompassed several sequential stages. In the initial phase, the feed solution was prepared and introduced into Feed Tank No. 1, consisting of a low TC concentration (1 mg L^{-1}) and Minghu Lake water were used as the reaction matrix. Subsequently, the focus shifted to achieving dynamic equilibrium in the flow rates across the system. This entailed calibrating the flow rates of Peristaltic Pumps to ensure a uniform water flow in and out of the entire setup. This step established the foundation for the ensuing process. The third step involved fine-tuning the inflow and outflow rates to control the hydraulic retention time. Once the reactor's water level reached a stable equilibrium of 5 hours, the subsequent phase was initiated. In this fourth step, 50 mg of the photocatalyst was introduced into Reactor No. 4 at a magnetic stirred speed of 500 rpm. Following a two-hour establishment of adsorption-desorption equilibrium in the absence of light, the illumination source was activated. The visible-light source was provided by a 300 W Xenon lamp equipped with a AM1.5 cutoff filter (Beijing China Education Au Light, Co., Ltd.). Lastly, the fifth stage encompassed the collection of treated water samples, subsequently subjected to HPLC analysis for degradation concentration measurement. Continuous flow system were performed at I = 100 mW cm^{-2} (AM 1.5G equivalent), Q = 10–50 mL min^{-1}, Vreactor = 1L, with HRT, 33, 50, 100(min).

Supplementary text 13.LC-MS

LC-MS analysis was performed to qualitatively detect tetracycline residues in C-N-La catalyst samples using a Thermo Scientific Ultimate 3000 UHPLC-Q Exactive hybrid quadrupole-orbitrap mass spectrometer (USA). Samples were filtered through a 0.22μm microporous membrane prior to direct injection.

Chromatographic Conditions: The chromatographic separation was conducted on a Dionex Ultimate 3000 UHPLC system equipped with a Zorbax Eclipse Plus C18 column (100 mm × 2.1 mm, 1.8 μm particle size) was maintained at a column temperature of 30°C. An injection volume of 10 μL was used, with mobile phase A consisting of 0.1% formic acid in water and mobile phase B as chromatographic-grade acetonitrile, delivered at a flow rate of 0.30 mL/min. The gradient elution program proceeded as follows: initial hold at 95% A and 5% B for 0–1 min, followed by a linear ramp to 83% A and 17% B over 1–5 min, then to 70% A and 30% B by 8 min, a steep increase to 10% A and 90% B at 12 min (held until 17 min), and finally re-equilibration to 95% A and 5% B from 17.2 min to 20 min. This ensured efficient resolution of target analytes within the 20-minute run time.

Gradient Elution:

Time(min)	A(%)	B(%)
0	95	5
1	95	5
5	83	17
8	70	30
12	10	90
17	10	90
17.2	95	5
20	95	5

Mass Spectrometry Conditions: Mass spectrometric detection was achieved using a Thermo Scientific Q Exactive orbitrap analyzer in positive ion mode with a heated electrospray ionization (HESI) source. Key parameters included a sheath gas flow of 40 arb, an auxiliary gas flow of 10 arb, a spray voltage of +3.8 kV, a capillary temperature of 320℃, an auxiliary gas temperature of 350°C, and an S-Lens RF level of 50%. Data acquisition employed a Full MS/dd-MS^2 top 10 scan mode, where the MS^1 stage operated at a resolution of 70,000 over an m/z range of 50–600, and the MS^2 stage utilized a resolution of 17, 500, with the collision energy starting at 50 m/z and normalized collision energies (NCE) stepped at 15, 30 and 45 eV for comprehensive fragmentation patterns. This configuration enabled high-resolution identification of tetracycline fragments via extracted ion chromatograms and tandem spectra.

Supplementary Text 13.Computational details

All calculations were carried out with the Gaussian software. The B3LYP functional[2] was adopted for all calculations in combination with the D3BJ dispersion correction[3].During the geometry optimization, the def2-SVP basis set[4] was employed for C, N, and H atoms, while the Stuttgart/Dresden (SDD)[5] effective core potential and its associated basis set were used for the La atom. The wave function analysis and visualization are performed by Multiwfn[6] and VMD[7],respectively. We have employed the VASP to perform all the spin-polarized density functional theory (DFT) calculations within the generalized gradient approximation (GGA) using the Perdew-Burke-Ernzerhof (PBE) formulation. We have chosen the projected augmented wave (PAW) potentials to describe the ionic cores and take valence electrons into account using a plane wave basis set with a kinetic energy cutoff of 400eV. Partial occupancies of the Kohn−Sham orbitals were allowed using the Gaussian smearing method and a width of 0.05 eV. The electronic energy was considered self-consistent when the energy change was smaller than 10^{-5} eV. A geometry optimization was considered convergent when the force

change was smaller than -0.05 eV/Å^2. Grimme's DFT-D3 methodology was used to describe the dispersion interactions among all the atoms. During structural optimizations of the surface models, the 2×2×1 gamma-point centered k-point grid for Brillouin zone was used.

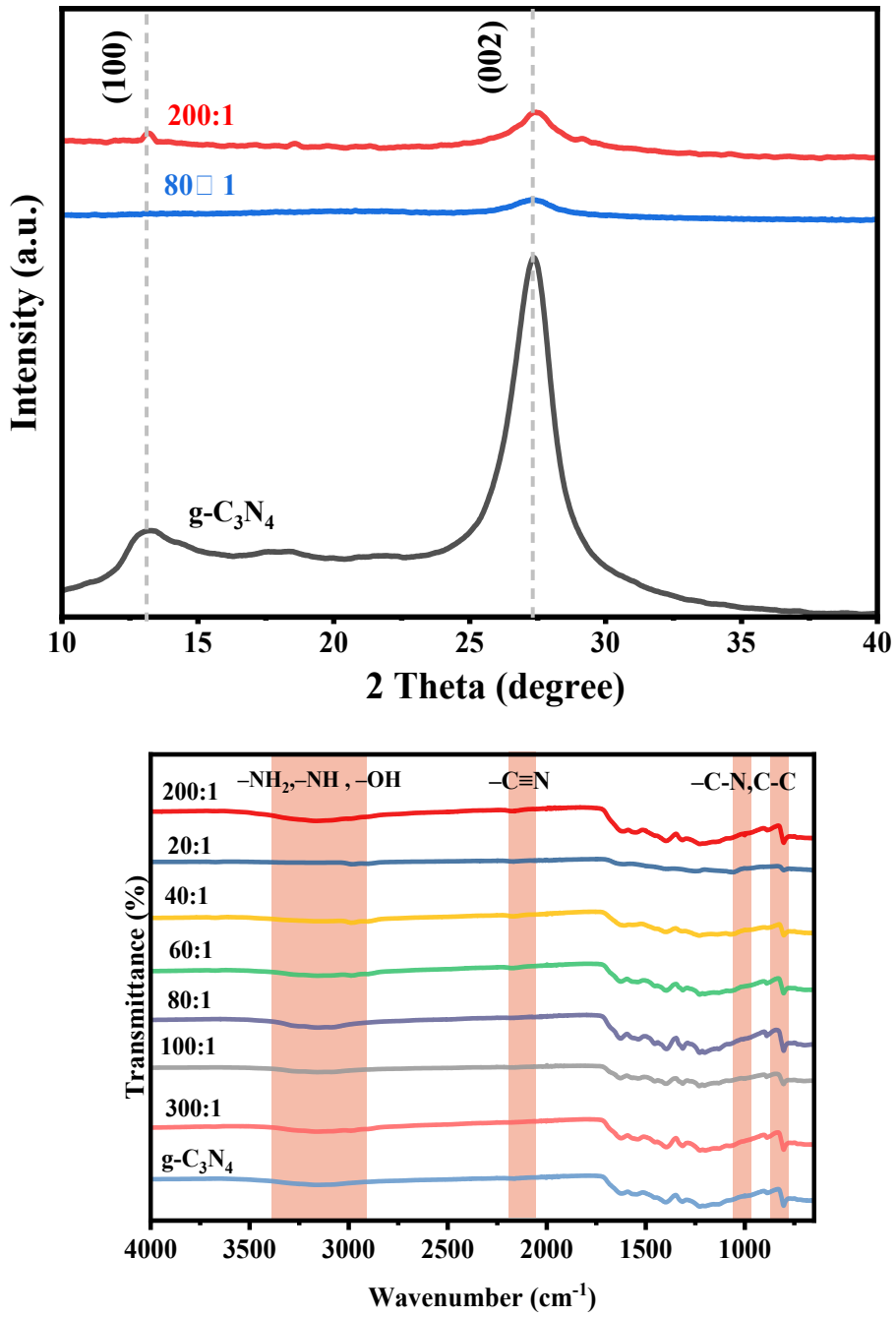

Supplementary Figure 4. X-ray diffraction (XRD) patterns of *g*-C_3N_4 and its composites and Fourier transform infrared (FT-IR) spectra of *g*-C_3N_4 and samples with different component ratios.

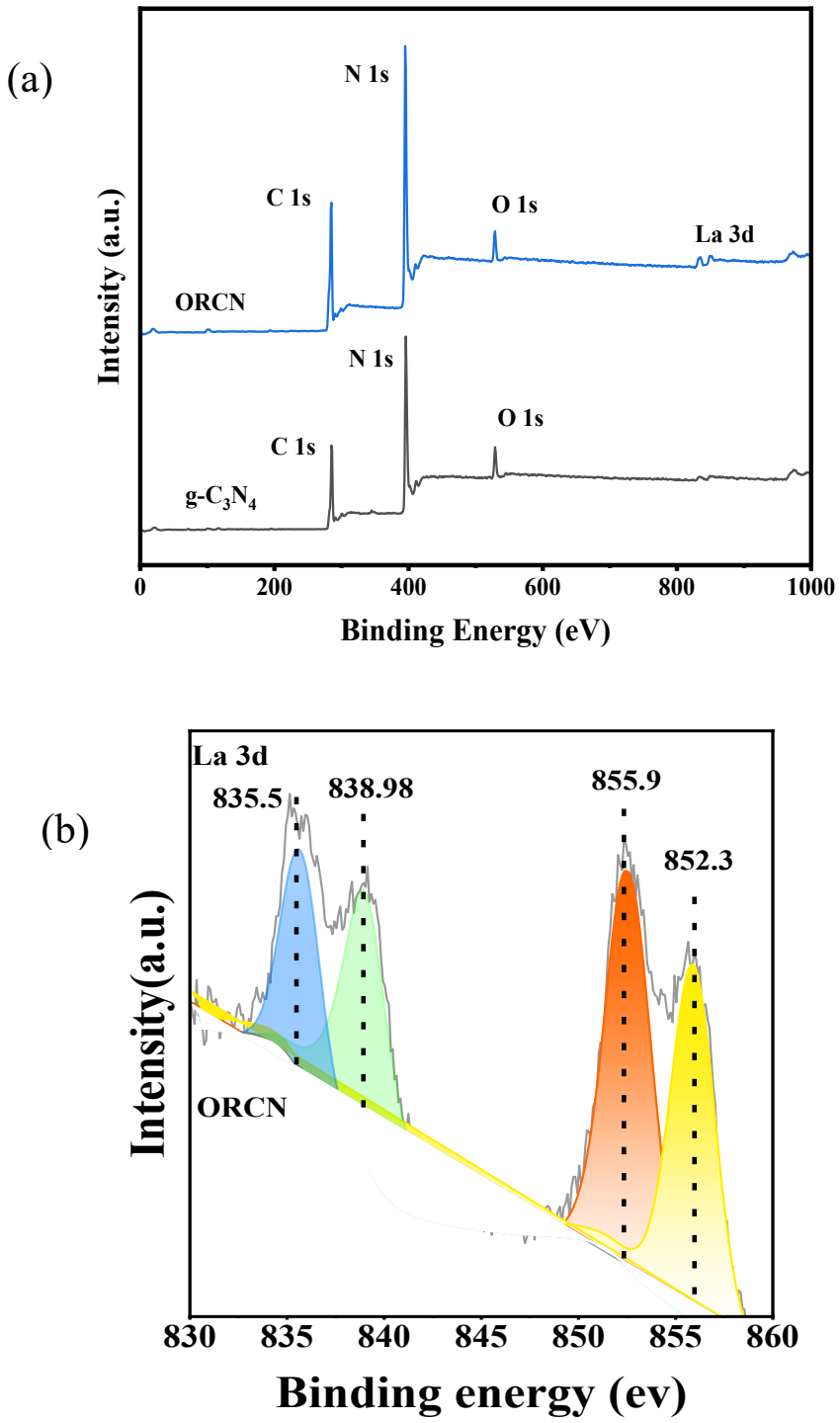

Supplementary Figure 5. (a) X-ray photoelectron spectroscopy (XPS) survey spectra of *g*-C_3N_4 and (b) ORCN and High-resolution XPS spectra of La 3d for and ORCN.

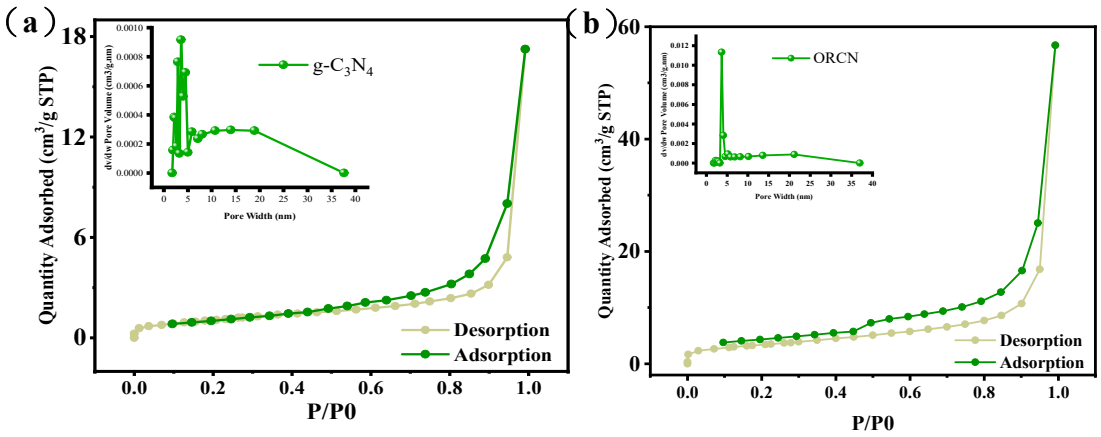

Supplementary Figure 6. Nitrogen adsorption-desorption isotherms for (a) g-C_3N_4 and (b) ORCN and the inset shows the pore size distribution.

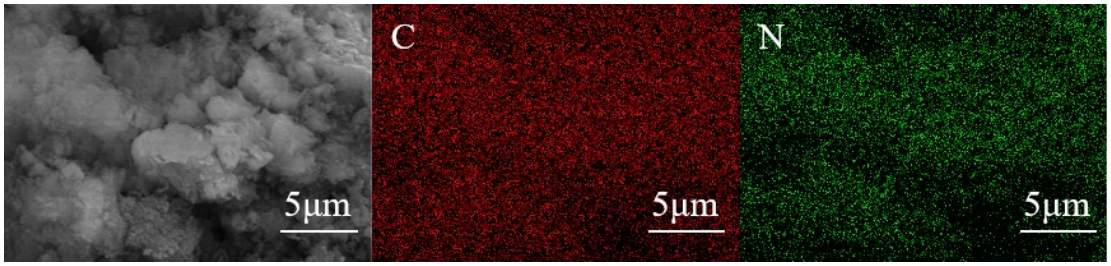

Supplementary Figure 7. SEM and EDS images of g-C3N4

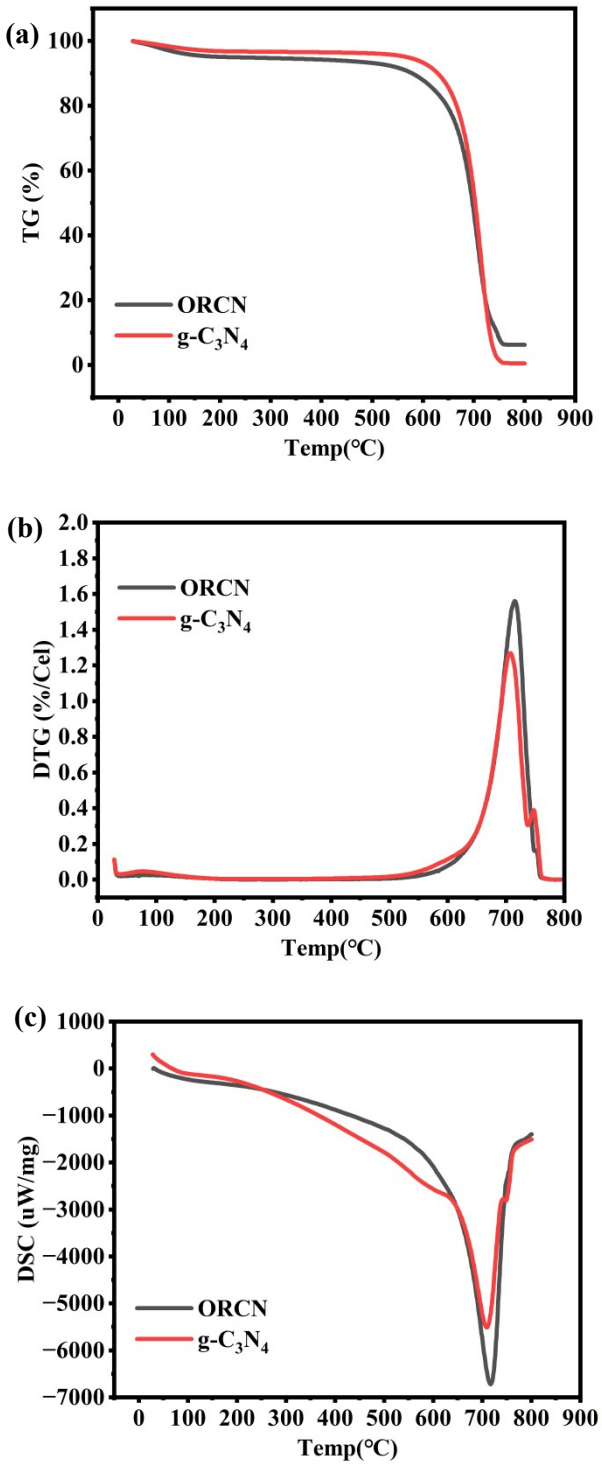

Supplementary Figure8. (a) Thermogravimetric (TG) curves comparison of ORCN and g-C_3N_4 (b) Differential scanning calorimetry (DSC) curves comparison of ORCN and g-C_3N_4 (c) Derivative thermogravimetric (DTG) curves comparison of ORCN and g-C_3N_4

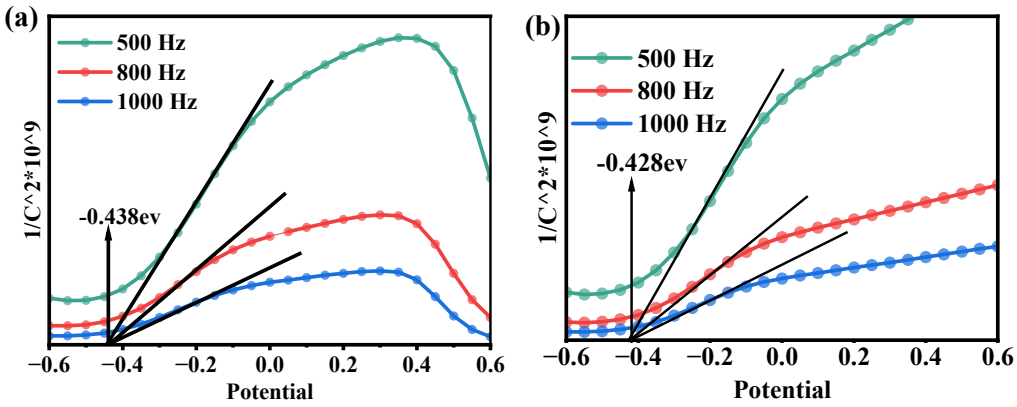

Supplementary Figure9. (a) Mott-Schottky curve of g-C_3N_4 (b) Mott-Schottky curve of ORCN.

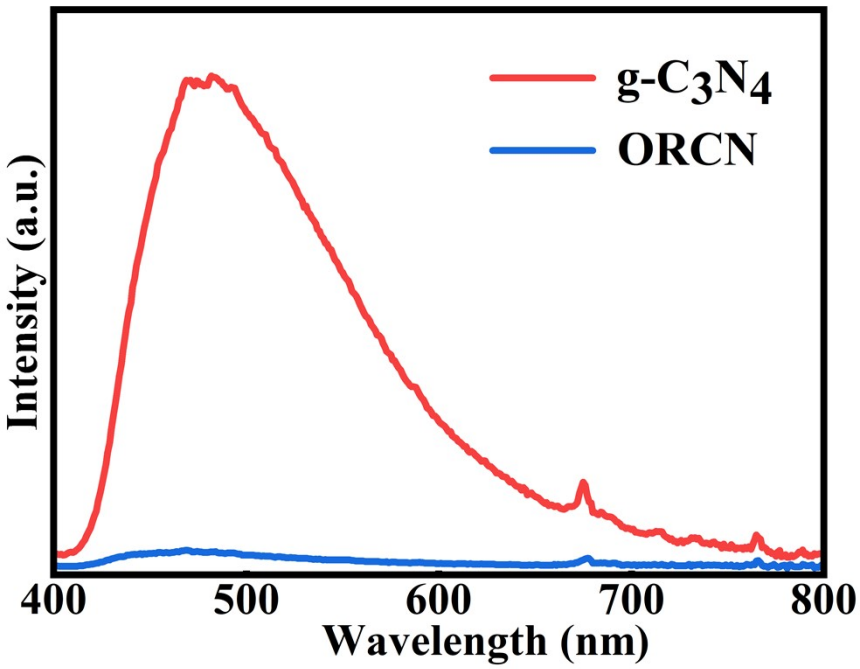

Supplementary Figure 10. Photoluminescence (PL) spectra of g-C_3N_4 and ORCN (λ=375 nm).

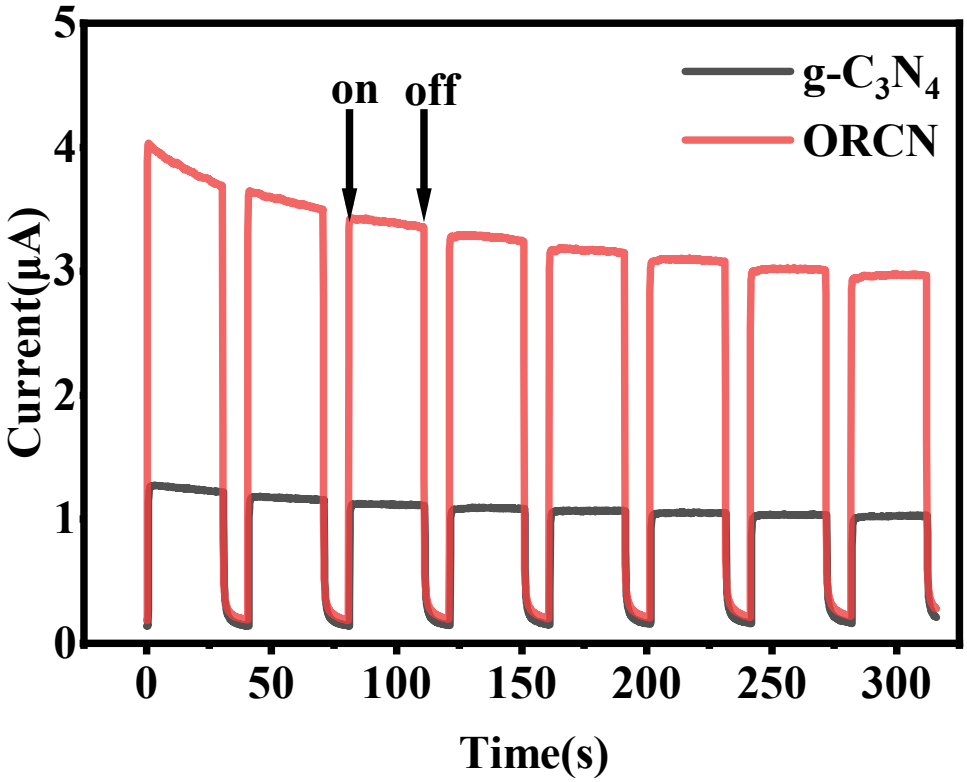

Supplementary Figure 11. Photocurrent responses of g-C_3N_4 and ORCN under intermittent visible light irradiation.

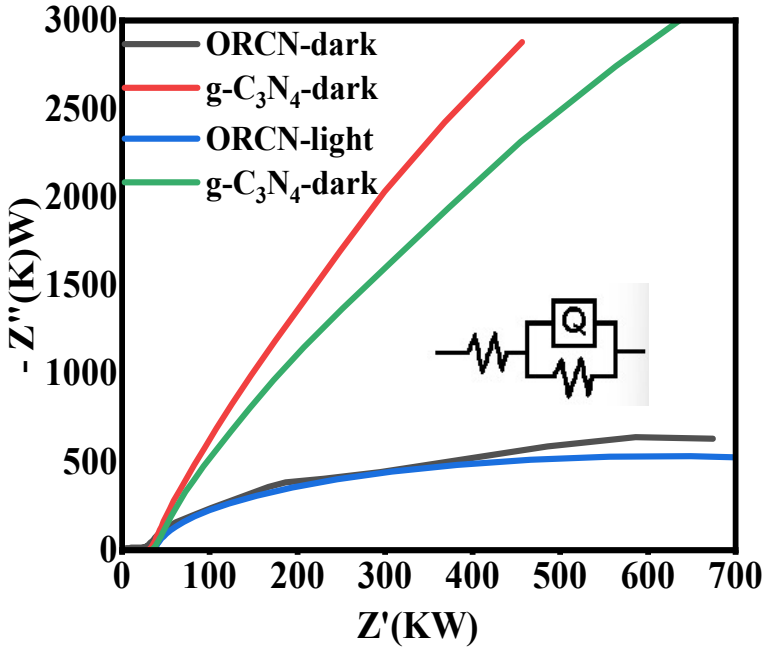

Supplementary Figure 12. EIS diagrams of g-$C_3N_4$and ORCN under light and dark conditions.

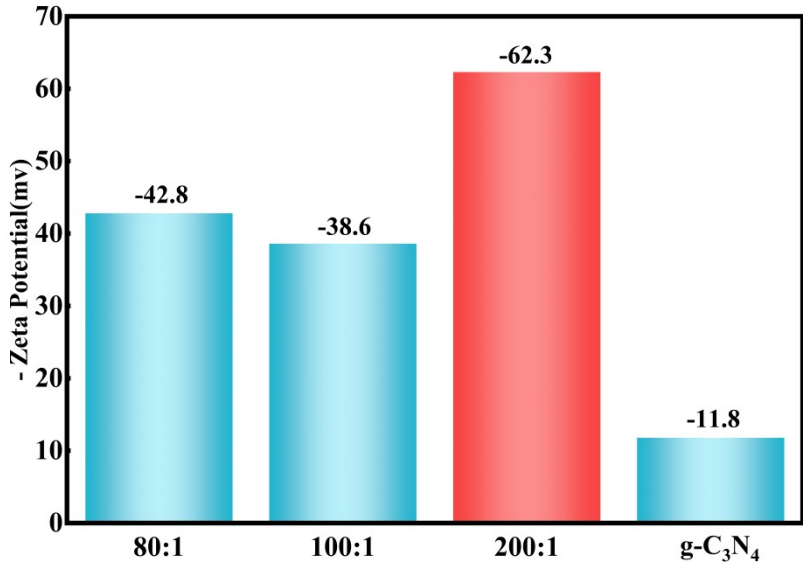

Supplementary Figure 13. Zeta potentials of g-C_3N_4 and carbon nitrides synthesized with different ratios

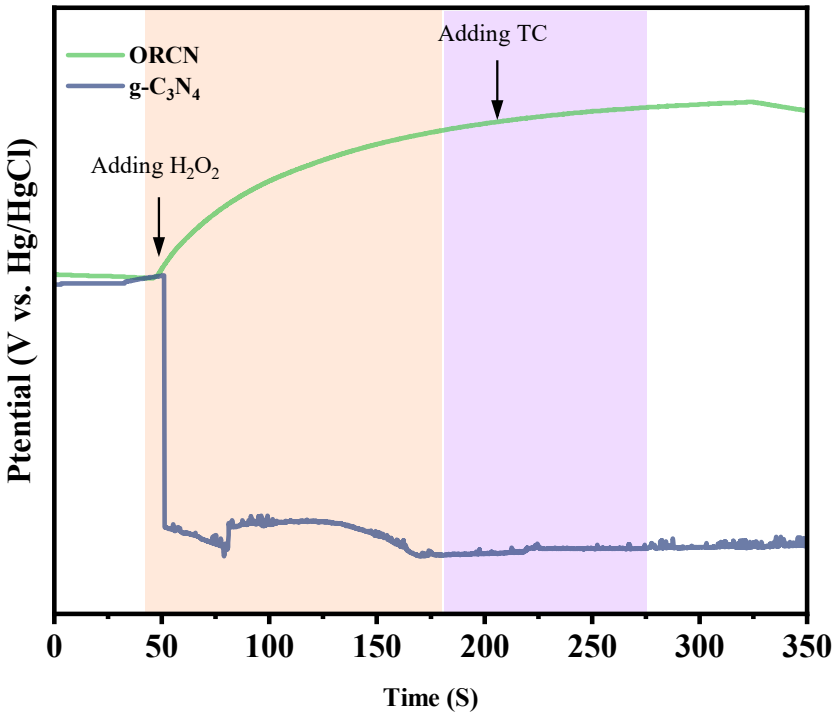

Supplementary Figure 14. Open-circuit potential (OCP) curves of ORCN and g-C_3N_4 upon adding TC and H_2O_2 sequentially.

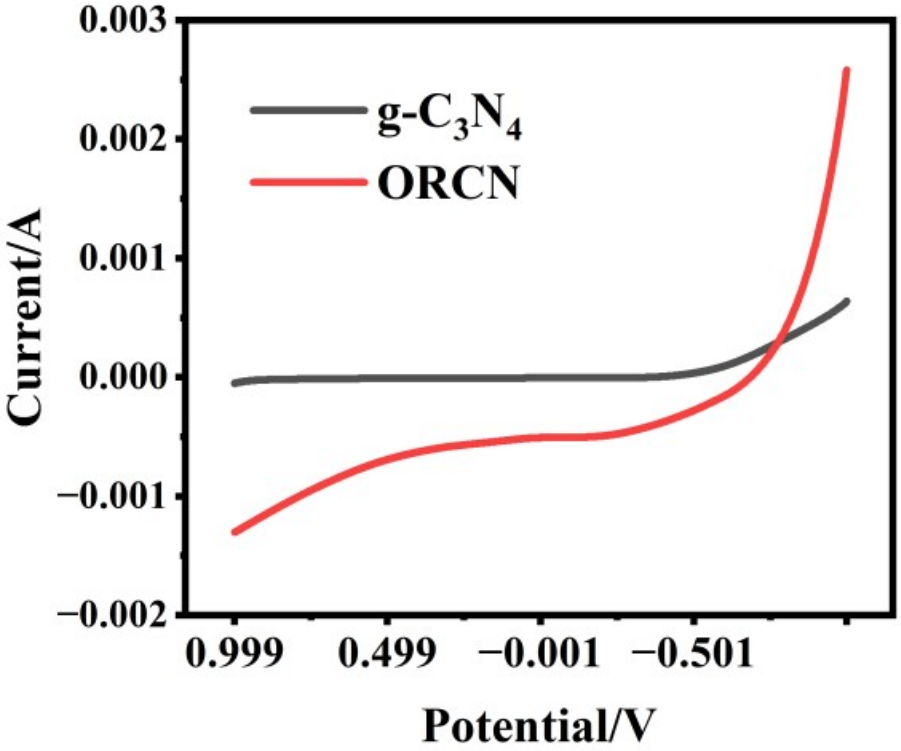

Supplementary Figure 15. LSV curves of ORCN and g-C_3N_4.

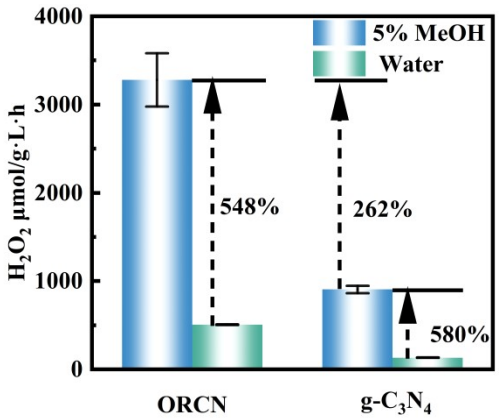

Supplementary Figure 16. Photocatalytic H_2O_2 production over ORCN and g-C_3N_4 in 5% MeOH aqueous solution and pure water. The dashed lines indicate the percentage increase in H_2O_2 yield relative to the corresponding control group (water for ORCN, 5% MeOH for g-C_3N_4).

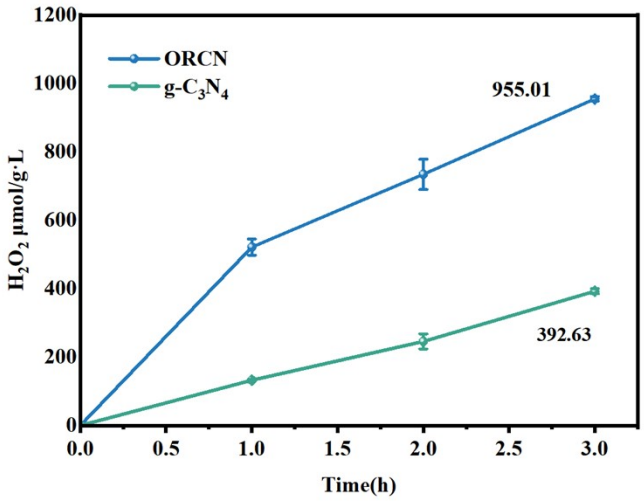

Supplementary Figure 17. Time-dependent photocatalytic H_2O_2 production over ORCN and g-C_3N_4. The curves illustrate the H_2O_2 yield (μ mol • g^{-1}) as a function of reaction time, with ORCN achieving 955.01 μ mol • g^{-1} and g-C_3N_4 reaching 392.03 μ mol • g^{-1} at 3.0 h, respectively.

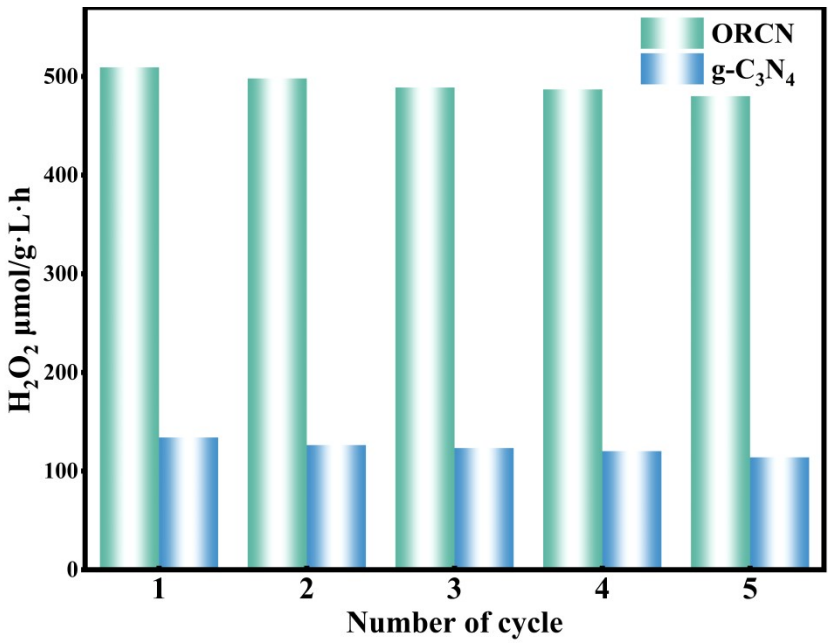

Supplementary Figure 18. Cycling stability of photocatalytic H_2O_2 production over ORCN and g-C_3N_4 across five reaction cycles.

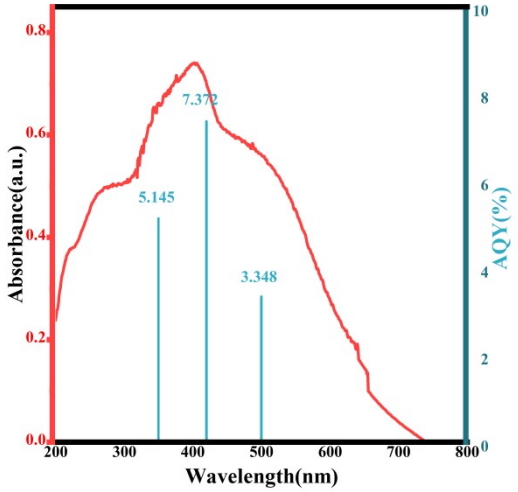

Supplementary Figure 19. UV–vis diffuse reflectance spectrum of the photocatalyst (red curve) and the corresponding apparent quantum yield (AQY) as a function of wavelength (blue bars).

λ=380 nm:

The number of incident photons:

$$N = \frac{ISt\lambda}{hc} = \frac{0.221 \times 2.12 \times 10^{-3} \times 3600 \times 380 \times 10^{-9}}{6.626 \times 10^{-34} \times 3 \times 10^{8}} = 3.22 \times 10^{18}$$

AQY:

$$\text{AQY} = \frac{2 \times number\ of\ produced\ H_2O_2\ molecules}{N} \times 100\% = \frac{2 \times 6.02 \times 10^{23} \times 0}{3.22 \times 10}$$
$$= 5.145\%$$

λ=420 nm:

The number of incident photons:

$$N = \frac{ISt\lambda}{hc} = \frac{0.263 \times 2.12 \times 10^{-3} \times 3600 \times 420 \times 10^{-9}}{6.626 \times 10^{-34} \times 3 \times 10^{8}} = 4.24 \times 10^{18}$$

AQY:

$$\text{AQY} = \frac{2 \times number\ of\ produced\ H_2O_2\ molecules}{N} \times 100\% = \frac{2 \times 6.02 \times 10^{23} \times 0}{4.24 \times 10}$$
$$= 7.372\%$$

λ=500 nm:

The number of incident photons:

$$N = \frac{ISt\lambda}{hc} = \frac{0.376 \times 2.12 \times 10^{-3} \times 3600 \times 500 \times 10^{-9}}{6.626 \times 10^{-34} \times 3 \times 10^{8}} = 7.22 \times 10^{18}$$

AQY:

$$\text{AQY} = \frac{2 \times number\ of\ produced\ H_2O_2\ molecules}{N} \times 100\% = \frac{2 \times 6.02 \times 10^{23} \times 0}{7.22 \times 10}$$

$$= 3.348\%$$

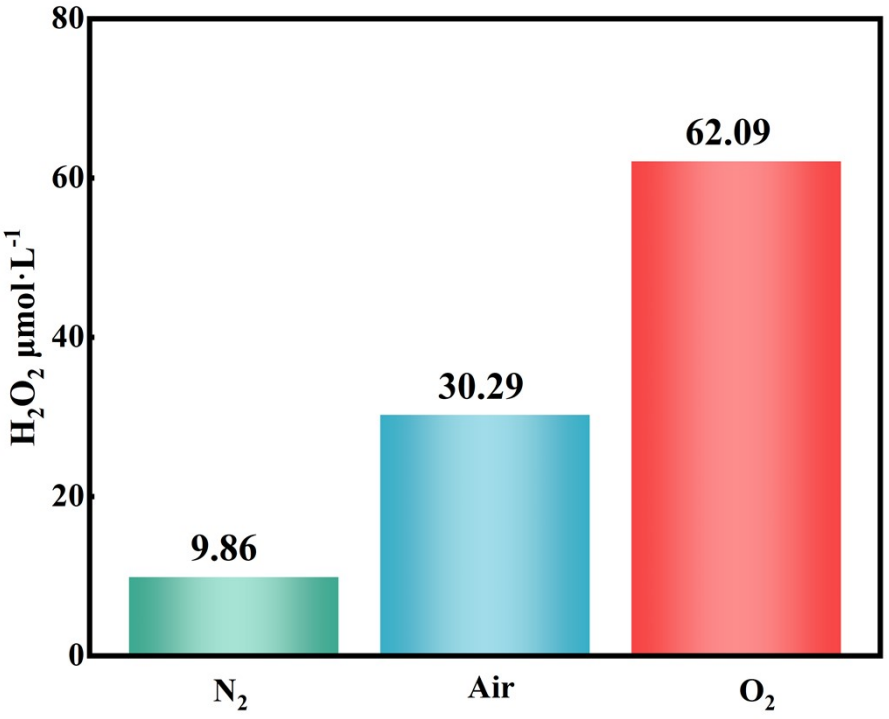

Supplementary Figure 20. H_2O_2 yields under N_2, air, and O_2 atmospheres.

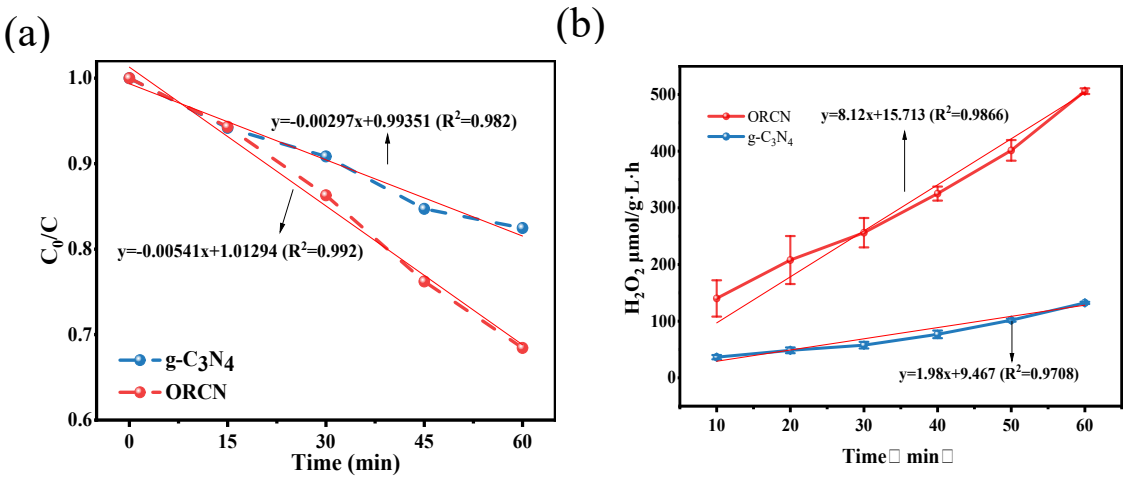

Supplementary Figure 21. g-C_3N_4 and ORCN decompose hydrogen peroxide and produce hydrogen peroxide.

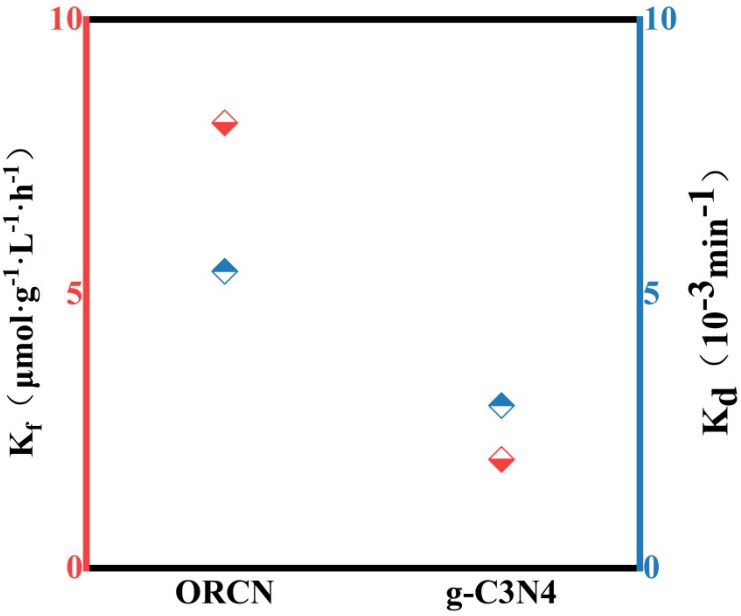

Supplementary Figure 22. H_2O_2 formation (K_f) and decomposition (K_d) rate constants of ORCN and g-C_3N_4.

Supplementary Figure 23. Apparent rate constants of target substances and corresponding concentration-time curves for g-C_3N_4-based materials at different synthesis ratios

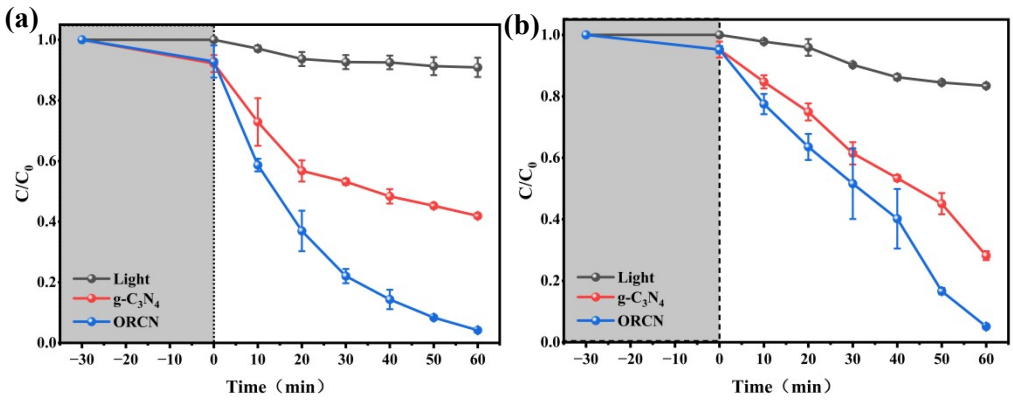

Supplementary Figure 24. g-C_3N_4, ORCN and simple light irradiation all exhibit degradation effects on sulfamethoxazole (a) and ciprofloxacin (b).

ORCN-200:1 exhibits superior photocatalytic oxidation efficiency, achieving a TC degradation rate constant of 12.8 × 10^{-2} min^{-1}—3.2× higher than g-C_3N_4—and >95% removal within 1 h, accompanied by a 73.4% TOC reduction (Fig. S20, Table S6). High degradation efficiencies are likewise obtained for ciprofloxacin and sulfamethoxazole (>97%, Fig. S21). The optimal catalyst dosage is 0.3 g L^{-1}, and ~80% activity is retained after five cycles (Fig. S22–S23). ORCN remains highly effective in tap and lake water (Fig. S24), showing strong resistance to matrix effects; although ions such as HCO_3^- and NOM inhibit performance via radical quenching and competitive adsorption (Fig. S25), removal efficiency remains high. ORCN exhibits optimal activity at pH=5 and consistently outperforms g-C_3N_4 across a broad pH range (Fig. S26).

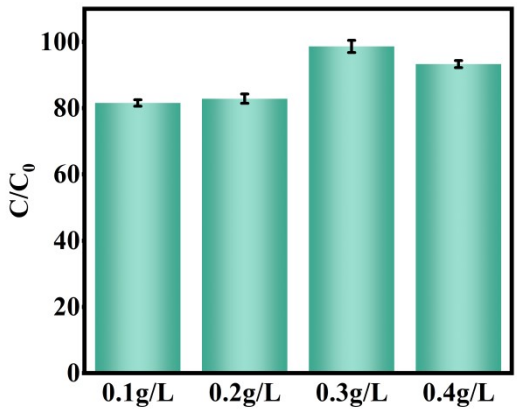

Supplementary Figure 25. Relative concentrations (C/C_0) of target substances under varying material dosages

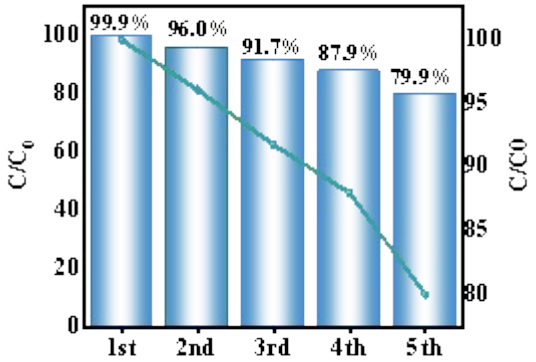

Supplementary Figure 26. Material recycling performance, illustrating C/C_0 values and corresponding trends across different recycling cycles

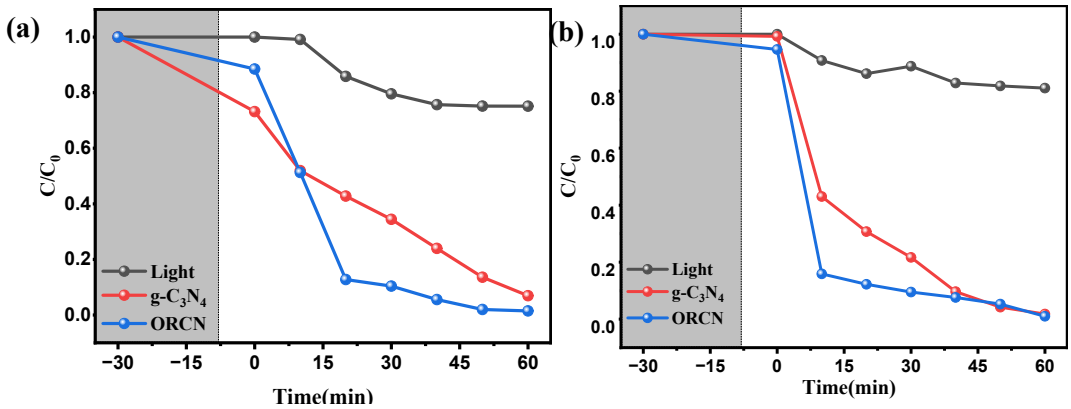

Supplementary Figure 27. Degradation of tetracycline by g-C_3N_4 and ORCN under light irradiation in tap water (a) and lake water backgrounds (b)

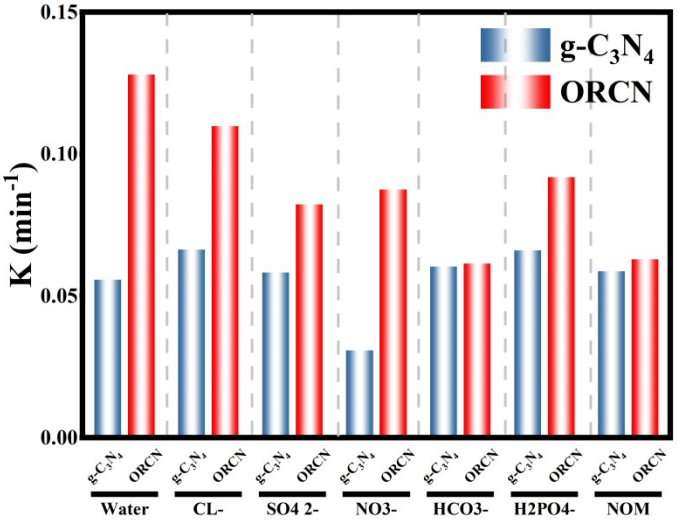

Supplementary Figure 28. Degradation rate constants of g-C_3N_4 and ORCN under varying influencing conditions. The concentrations of inorganic ions were determined according to the composition of surface water in Beijing: [Cl^-] = 135.3 mg/L, [SO_4^{2-}] = 124.0 mg/L, [NO_3^-] = 13.6 mg/L, [HCO_3^-] = 272.0 mg/L, and [$H_2PO_4^-$] = 5.0 mg/L. The natural organic matter (NOM) content in surface water typically ranges from 1 to 10 mg/L. In this study, humic acid (HA) was selected as a representative NOM at 10 mg/L.

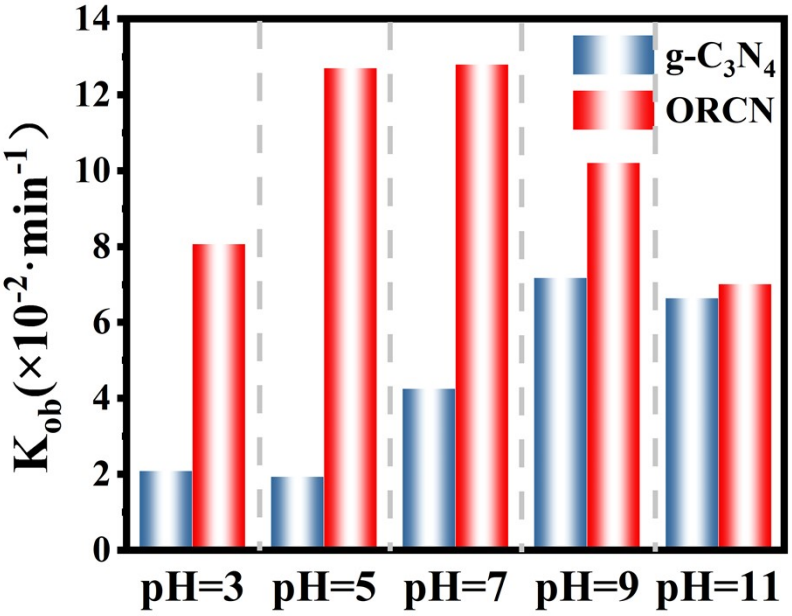

Supplementary Figure 29. Apparent rate constants of g-C_3N_4 and ORCN at different pH conditions.

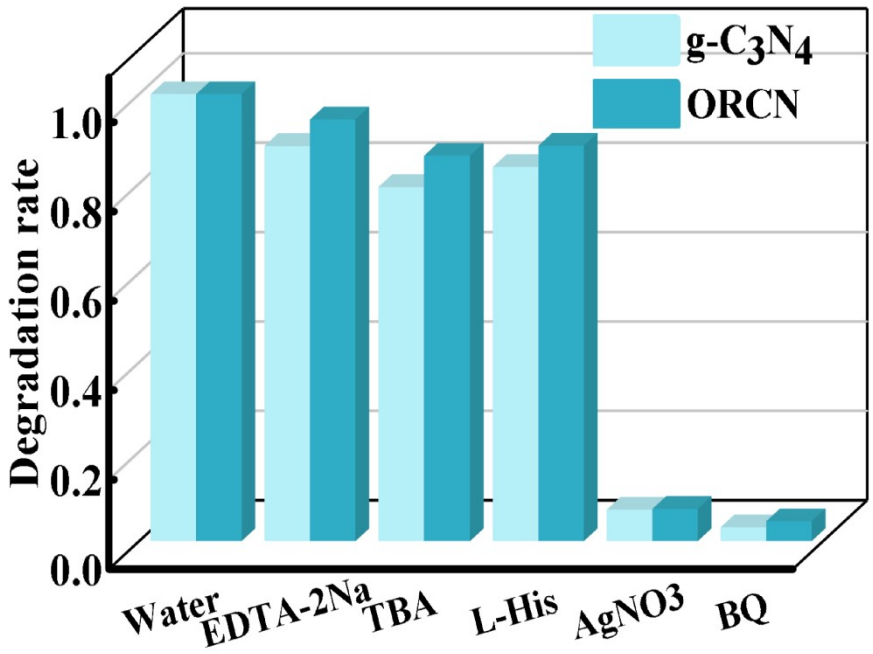

Supplementary Figure 30. Degradation rates of the target substance by g-C_3N_4 and ORCN in the presence of different scavengers.

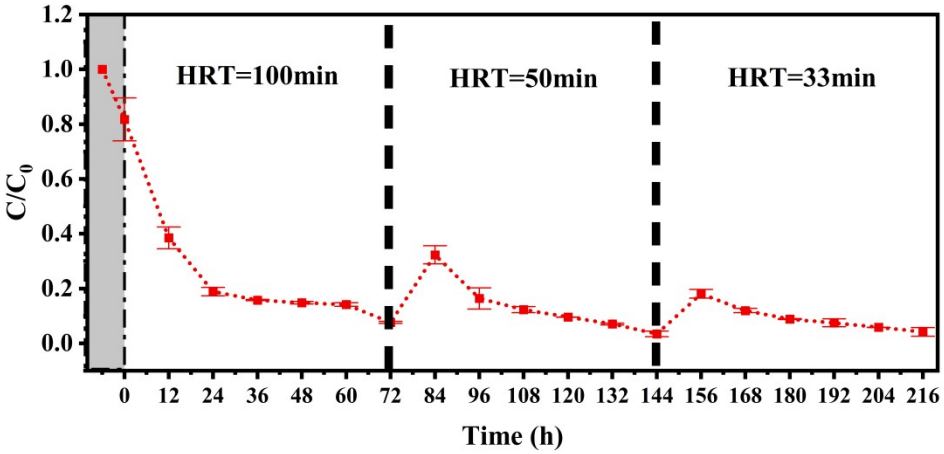

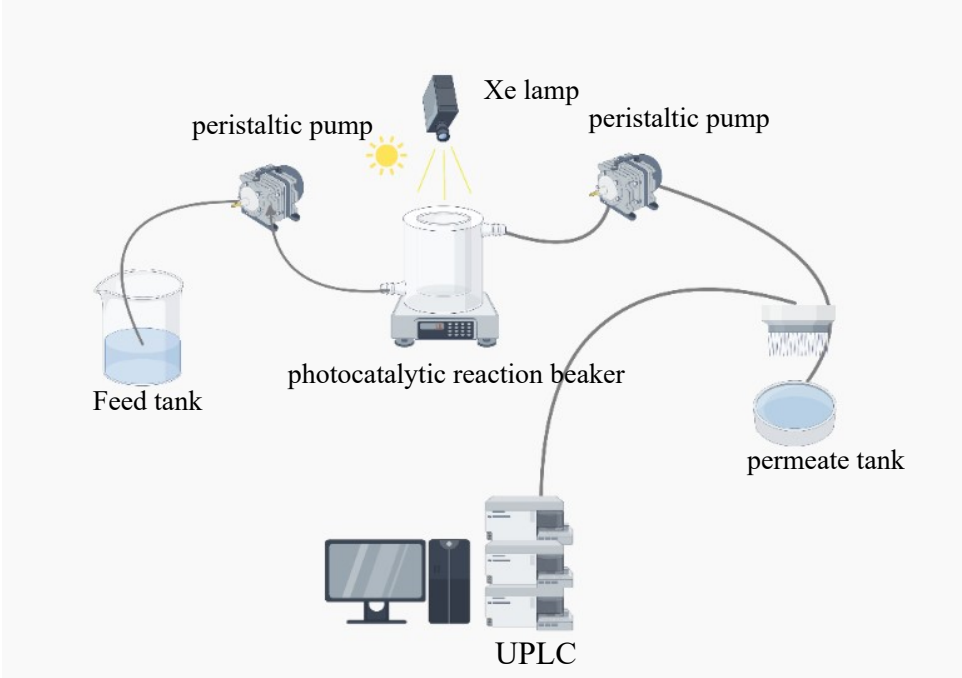

Supplementary Figure 31. Degradation of ORCN in continuous flow apparatus and schematic diagram of the device

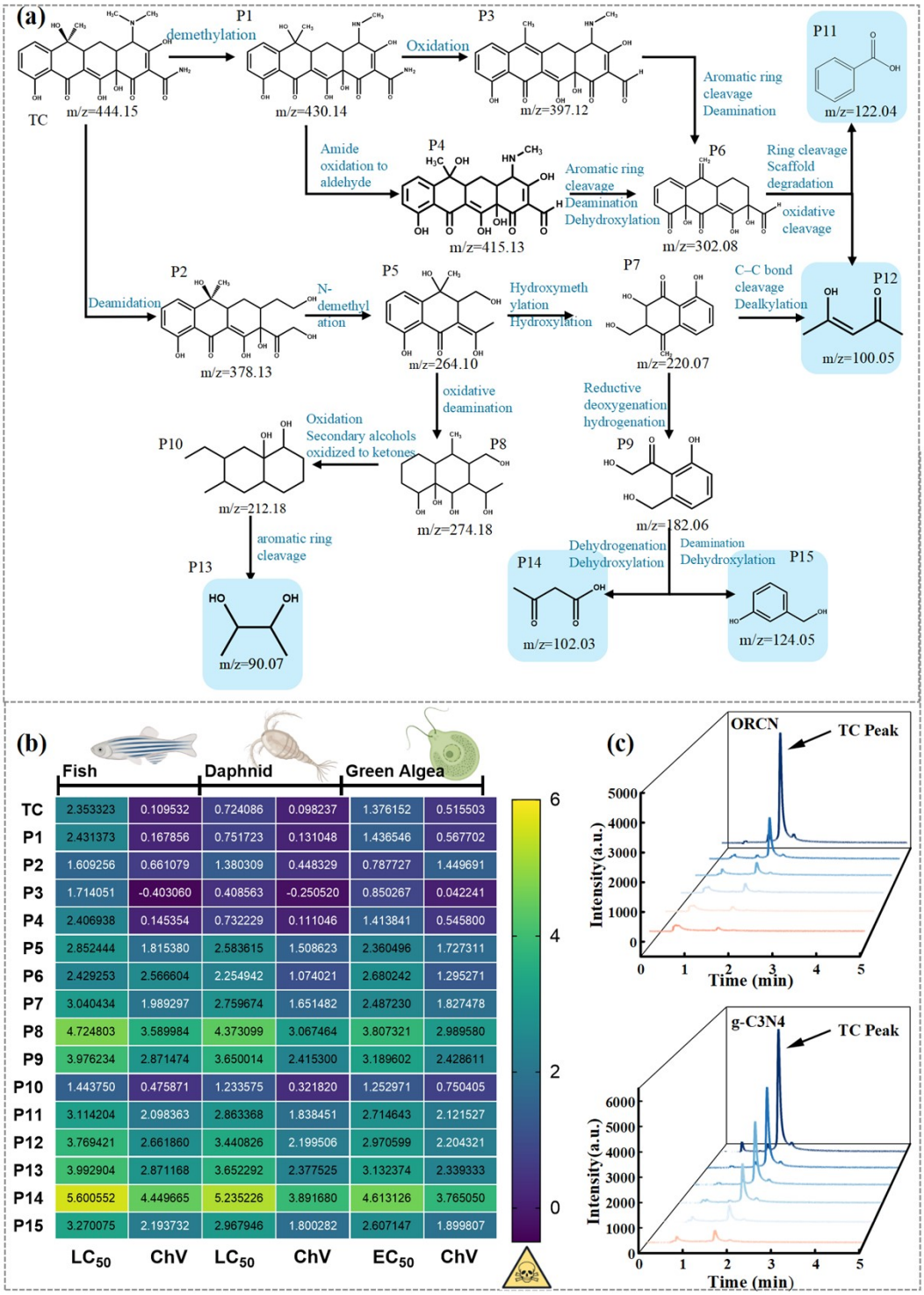

Supplementary Figure 32. (a)Degradation pathways of tetracycline degradation intermediates as analysed by high-performance liquid chromatography-mass spectrometry (HPLC-MS); (b)Toxicity assessment data for tetracycline and its degradation intermediates, including half-effect concentration (EC_{50}), lethal concentration (LC_{50}), and chronic toxicity (CV) data for the following organisms: algae, Daphnia, and fish; (c)UPLC profiles of tetracycline degradation by ORCN and g-C_3N_4.

TC (m/z 444.15) initially undergoes demethylation to P1 (m/z 417), followed by ring opening, deamination and β-diketone cleavage to generate intermediates such as P2 (m/z 378.13) [4], P5 (m/z 264.10), P7 (m/z 220.07) and P8 (m/z 274.18). Further oxidation yields low-molecular-weight species, indicative of progressive fragmentation leading to near-complete mineralisation[5]. The high density of La-centred Lewis acid sites enhances ·OH formation, accelerating C–N and C–C bond rupture. Ecotoxicity evaluation using ECOSAR (**Fig. S29b, Table S10**) reveals that pristine TC poses considerable acute risk to aquatic organisms, particularly daphnids. Both acute and chronic toxicity decrease markedly during photocatalysis, and final products are essentially non-toxic. Metal-leaching tests (**Table S9**) show that La release remains below 0.03 mg L^{-1}, far lower than WHO and US EPA limits, confirming high structural stability and negligible risk of secondary contamination.

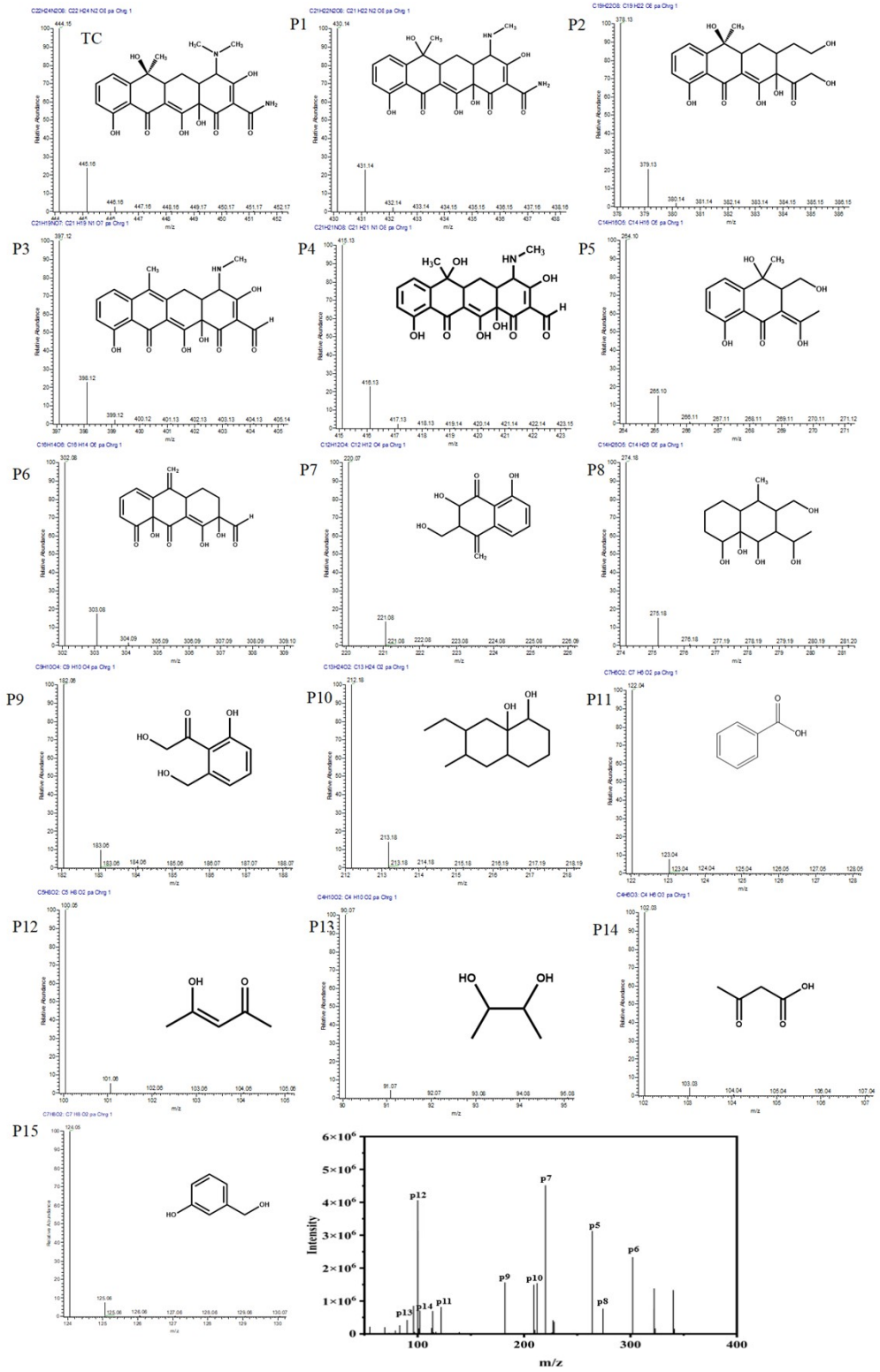

Supplementary Figure 33. LC-MS

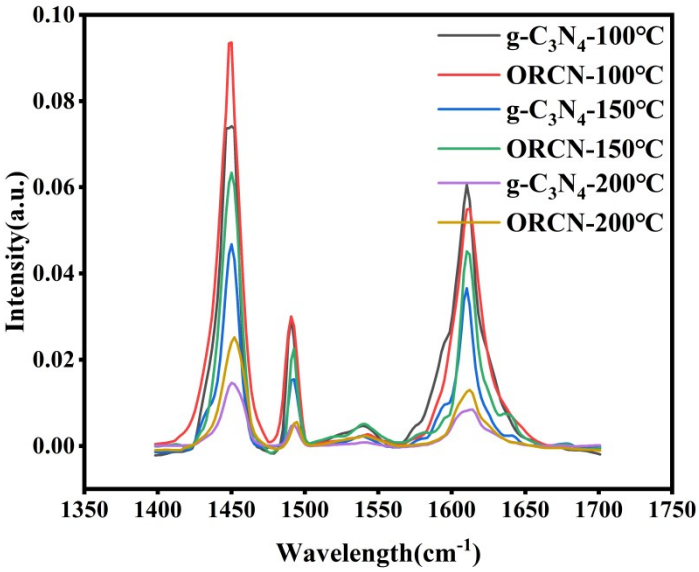

Supplementary Figure 34. Pyridine FT-IR Spectra of g-C_3N_4 and ORCN at 100℃、150°C、 200°C.

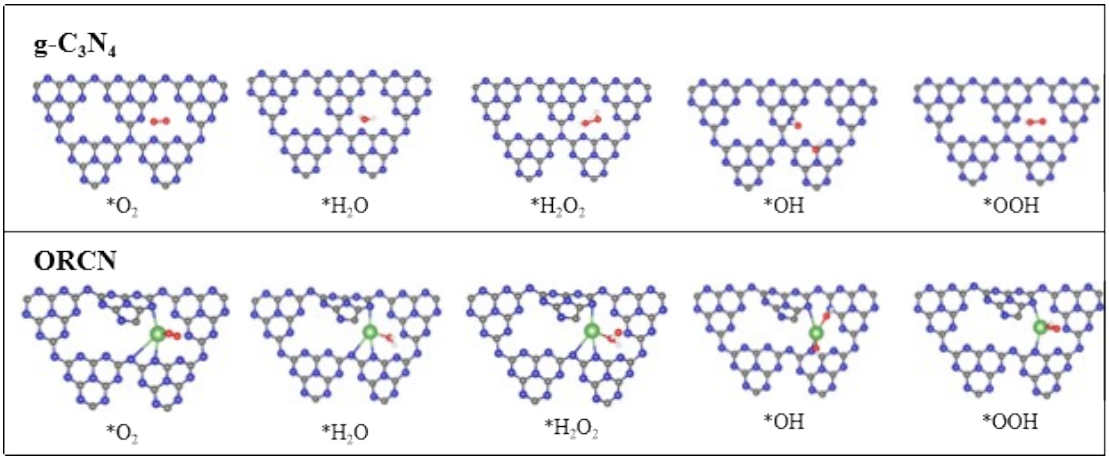

Supplementary Figure 35.*O_2, *OOH, *H_2O_2 and *OH structures of g-C_3N_4 and ORCN.

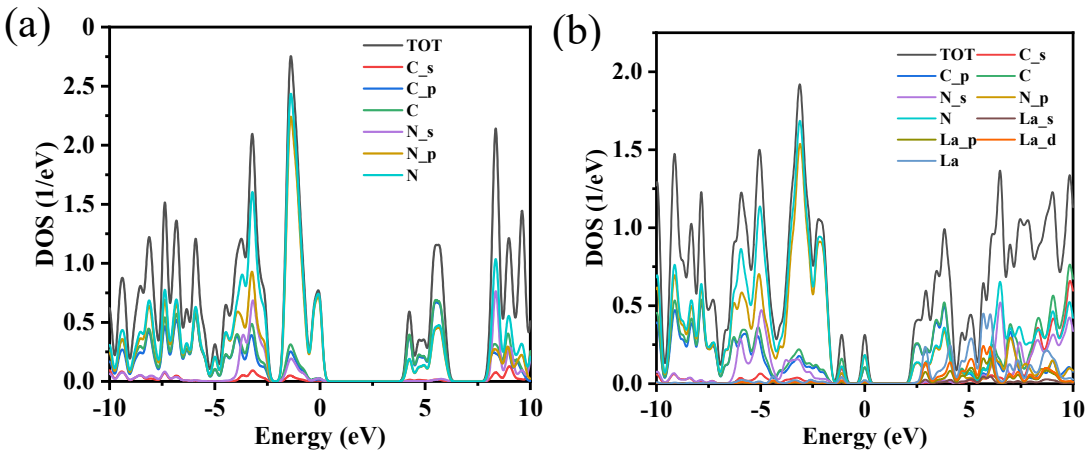

Supplementary Figure 36: (a)Density of states (DOS) for g-C_3N_4, displaying the total density of states (TOT) and the orbital density of states for C and N atoms. (b)Density of states for ORCN, displaying the total density of states and the orbital density of states for C, N, and La atoms.

Table S1. The BET specific surface area, pore volume, and specific surface area of g-C_3N_4 and ORCN.

Bet	Pore volume	Specific surface area
ORCN	0.0807ml/g	12.2184㎡/g
g-C_3N_4	0.0244ml/g	4.3767㎡/g

Table S2. Atomic percentage (%) of various bonding configurations (C-C, C-N, N-C=N, C-N=C, N-$(C)_3$, C-N-H, π excitation) in g-C_3N_4 and ORCN samples.

Sample	**C1(%)**	**C2(%)**	**C3(%)**	**N1(%)**	**N2(%)**	**N3(%)**	**N4(%)**
	C-C	**C-N**	**N-C=N**	**C-N=C**	**N-$(C)_3$**	**C-N-H**	**πexcitation**
g-C_3N_4	15.43	3.30	81.27	52.33	34.08	6.75	6.84
ORCN	19.90	4.34	75.76	43.50	39.61	10.23	6.66

Table S3. Atomic percentages (%) of C, N, La, and the C/N ratio for g-C_3N_4 and ORCN samples.

Sample	C(%)	N(%)	La(%)	C/N(%)
g-C_3N_4	42.56	57.44	0.00	0.74
ORCN	45.02	54.76	0.22	0.82

Table S4. Dissolved oxygen concentration (mg/L) in deionized water and oxygen-exposed deionized water.

Dissolved oxygen（mg/L）	Deionized water	Oxygen-exposed deionized water
	4.81	8.79

Table S5. Electrical conductivity (μS/cm) of deionized water and Daming Lake Water.

Electrical conductivity（qS/cm）	Deionized water	Daming Lake Water
	2.45	1209

Table S6. TOC (mg/L) and removal efficiency of 5ppm TC Lake Water, and that after illuminating for 1 hour with ORCN and g-C_3N_4 added, respectively.

TOC（mg/L）	5ppmTC Lake Water	Illuminate for 1 hour after adding ORCN	Illuminate for 1 hour after adding g-C_3N_4
	48.24	12.83	20.65
Removal efficiency		73.40%	57.19%

Table S7. The SCC (%) of ORCN and g-C_3N_4 samples.

Sample	SCC（%）
ORCN	**0.87**
g-C_3N_4	**0.049**

Table S8. The concentrations (mg/L) of NH, TP, and TN in lake water before and after decomposition.

Water quality indicators（mg/L）	NH	TP	TN
Before the lake water degrades	0.072	0.083	1.37
After the lake water decomposes	0.058	0.038	1.03

Table S9. The lanthanum ion concentration (ppm) at 4h, 8h, and 12h.

Lanthanum ion concentration（ppm）	**4h**	**8h**	**12h**
	0.0292	0.0295	0.0295

Table S10. Toxicity classification criteria for ecotoxicity analysis.

Toxicity range($mg \cdot L^{-1}$)	Logarithmic-transformed toxicity range	Class
$K \leq 1$	$\lg k \leq 0$	Very toxic
$1 < k \leq 10$	$0 < \lg k \leq 1$	Toxic
$10 < k \leq 100$	$1 < \lg k \leq 2$	Harmful
$K > 100$	$\lg k > 2$	Not harmful

Table S11 Comparison of photocatalytic H_2O_2 production(1h)with other reported works.

Photocatalyst	Reaction solvent	Dosage (g/L)	Light source	H_2O_2 evolution (μmol L^{-1})	AQY	SCC (%)	Ref.
M-CN_T	pure water	1.0	(λ≥420 nm)	44.63μmol·L h^{-1}	/	/	6
HCN@PDA	pure water	0.2	(400 nm<λ<780nm)	23.25μmol·L h^{-1}	6.12%(λ=380 nm)	/	7
Pt/CN	pure water	1.0	(λ≥420 nm)	31.82μmol·L h^{-1}	/	/	8
PDA/SCN-3	pure water	0.2	（λ≥420 nm）	233μmol·L h^{-1}	11.3%(λ=420 nm)	/	9
Cv-g-C_3N_4	pure water	1.0	λ>420 nm	96μmol·L h^{-1}	/	/	10
DPCN-520	10%EtOH	1.0	λ>420 nm	283μmol·L h^{-1}	/	/	11
C_3N_4-nv	pure water	1.0	λ>420 nm	75.66μmol·L h^{-1}	/	/	12
CN-A	pure water	1.0	λ≥420 nm	147.2μmol·L h^{-1}	/	0.0936	13
AQ/CN-70%	pure water	1.0	λ≥420 nm	165.3μmol·L h^{-1}	2.48%(λ=420 nm)	/	14
CoOx-NvCN	pure water	1.0	λ≥420 nm	244.8μmol·L h^{-1}	5.73%(λ=420 nm)	0.47	15
ORCN	pure water	0.2	(λ≥420 nm)	505.9μmol·L h^{-1}	7.37%(420nm)	0.87	This work

Table S12 Comparison of photocatalytic H_2O_2 production performance (within 1 hour) with other reported metal-modified carbon nitride studies

Photocatalyst	Reaction solvent	Dosage (g/L)	Light source	H_2O_2 evolution	Ref.
Er-CN	**pure water**	**0.66**	**λ ≥ 420 nm**	**300.74 μmol·g^{-1}·h^{-1}**	[16]
10 wt% K+ ion doped g-C_3N_4	**pure water**	**4**	**λ ≥ 420 nm**	**200 μmol·g^{-1}·h^{-1}**	[17]
CoO_x-BCN-FeOOH	**pure water**	**1**	**λ ≥ 420 nm**	**340 μmol·g^{-1}·h^{-1}**	[18]
C_v-g-C_3N_4	**pure water**	**1**	**λ ≥ 420 nm**	**92 μmol·g^{-1}·h^{-1}**	[19]
NaClO-CN	**EtOH 10 *vol.* %**	**1**	**λ ≥ 420 nm**	**104 μmol·g^{-1}·h^{-1}**	[20]

Table S13. The Brown acid area, Lewis acid area, Brown acid quantity, Lewis acid quantity, total acidity, and B/L ratio of g-C_3N_4 and ORCN at temperatures of 100°C, 150°C, and 200°C.

Sample	Temperature (℃)	Brown acid area	Lewis acid area	Brown acid quantity（μmol/g）	Lewis acid quantity（μmol/g）	Total acidity（μmol/g）	B/L
g-C_3N_4	100	0.11	1.47	4.62291	46.66278	51.28569	0.099071
	150	0.06	0.755	2.521587	23.96626	26.48784	0.105214
	200	0.025	0.26	1.050661	8.25328	9.303942	0.127302
ORCN	100	0.156	1.91	6.626245989	61.27831551	67.9045615	0.108133618
	150	0.11	1.14	4.672352941	36.57449198	41.24684492	0.12774895
	200	0.062	0.56	2.633508021	17.96641711	20.59992513	0.146579477

References

1. M. T. Oo, Y. Zhao, S. Baqi, J. Zhou, M. T. Phoo and R.-Q. Zhang, *Small*, 2025, **21**, 2406430.
2. X. Bai, X. Liu and R. Zong, *Applied Catalysis B: Environment and Energy*, 2025, **366**, 125062.
3. M. Li, N. Chen, H. Shang, C. Ling, K. Wei, S. Zhao, B. Zhou, F. Jia, Z. Ai and L. Zhang, *Environmental Science & Technology*, 2022, **56**, 10945-10953.
4. G. Yang, Y. Liang, Z. Xiong, J. Yang, K. Wang and Z. Zeng, *Chemical Engineering Journal*, 2021, **425**, 130689.
5. S. Xin, S. Huo, C. Zhang, X. Ma, W. Liu, Y. Xin and M. Gao, *Applied Catalysis B: Environmental*, 2022, **305**, 121024.
6. J. Li, Y. Li, S. Wei, S. Wu, Z. Peng, F. Zhang, L. Huang, L. Chen, J. Li and H. Xiao, *Applied Catalysis B: Environment and Energy*, 2025, **366**, 125073.
7. L. Li, F. Ye, Q. Lv, J. Xia, N. Chen, H. Wang, L. Chen, K. Zhao, Z. Zeng, M. Ahmad, Z. Xiao, S. Wang and Q. Zhang, *Applied Catalysis B: Environment and Energy*, 2025, **363**, 124802.
8. L. Nie, H. Chen, J. Wang, Y. Yang and C. Fang, *Inorganic Chemistry*, 2024, **63**, 4770-4782.
9. Y. Li, Y. Wang, W. Wang, H. He, L. Zhang, L. Deng and Y.-N. Liu, *Applied Catalysis B: Environment and Energy*, 2025, **364**, 124863.
10. S. Li, G. Dong, R. Hailili, L. Yang, Y. Li, F. Wang, Y. Zeng and C. Wang, *Applied Catalysis B: Environmental*, 2016, **190**, 26-35.
11. J. Tian, B. Feng, X. Zhang, K. Gu, Y. Pei, M. Qiao, J. Zhang and B. Zong, *Journal of Colloid and Interface Science*, 2023, **634**, 138-147.
12. Y. Lu, Y. Guo, S. Zhang, L. Li, R. Jiang, D. Zhang, J. C. Yu and J. Wang, *ACS Nano*, 2024, **18**, 20435-20448.
13. S. Wu, Y. Li, S. Wei, J. Li, F. Zhang, J. Li, L. Huang, L. Chen and H. Xiao, *Chemical Engineering Journal*, 2025, **508**, 160890.
14. J. Li, W. Tian, S. Du, L. Wang, H. Zhang, Q. Chen, C. Zhou, L. Shang, G. Chen, T. Zhang and X. Meng, *Journal of Materials Chemistry A*, 2025, **13**, 36351-36360.
15. J. Hou, K. Wang, X. Zhang, Y. Wang, H. Su, C. Yang, X. Zhou, W. Liu, H. Hu, J. Wang, C. Li, P. Ma, R. Zhang, Z. Wei, Z. Sun, Q. Liu and K. Zheng, *ACS Catalysis*, 2024, **14**, 10893-10903.
16. K. Xie, D. Jiang, X. Xu, J. Hu, Y. Peng, S. Liu and H. Wen, *Journal of Rare Earths*, 2025, DOI: https://doi.org/10.1016/j.jre.2025.09.022.
17. P. Haripriya, T. Anjana, K. Sreelakshmi, N. T. Madhu, M. Anjana, P. V. Suneesh and D. V. Ravi Kumar, *Catalysis Communications*, 2024, **187**, 106909.
18. P. Liu, T. Liang, Y. Li, Z. Zhang, Z. Li, J. Bian and L. Jing, *Nature Communications*, 2024, **15**, 9224.
19. Z. Zhu, H. Pan, M. Murugananthan, J. Gong and Y. Zhang, *Applied Catalysis B: Environmental*, 2018, **232**, 19-25.
20. Y. Kofuji, S. Ohkita, Y. Shiraishi, H. Sakamoto, S. Ichikawa, S. Tanaka and T. Hirai, *ACS Sustainable Chemistry & Engineering*, 2017, **5**, 6478-6485.